Deep Learning-Aided Spatial Discrimination for Multipath Mitigation

Ali A. Abdallah* and Zaher M. Kassas*†
University of California, Irvine, U.S.A.
* Department of Electrical Engineering and Computer Science
† Department of Mechanical and Aerospace Engineering
Email: abdalla2@uci.edu, zkassas@ieee.org

***Abstract*—A deep learning-aided spatial discriminator for multipath mitigation is developed. The proposed system compensates for the limitations of conventional beamforming approaches, especially at the stages of: prefiltering, model order estimation (MOE), and direction-of-arrival (DOA) estimation. Three environments are considered to design and train the proposed deep neural networks (DNNs): indoor office buildings, indoor open ceiling, and outdoor urban area. The performance of the proposed DNN-based MOE is compared to the conventional approaches of minimum description length (MDL) criterion and Akaike information criterion (AIC). The proposed DNN-based MOE is shown to significantly outperform existing approaches and to increase the degrees-of-freedom. Four experiments are presented to assess the performance of the proposed system in multipath-rich environments corresponding to indoor pedestrian navigation and ground vehicle urban navigation with cellular long-term evolution (LTE) signals. The proposed system exhibited a position root mean-squared error (RMSE) of 1.67 m, 3.38 m, 1.73 m, and 2.16 m.**

***Index Terms*—Beamforming, multipath mitigation, DNN, navigation, synthetic aperture, LTE.**

I. Introduction

The ability to localize and navigate a user reliably and accurately is crucial for autonomous vehicles, public safety, location-based services (LBS) [1]. Existing navigation technologies can be broadly classified into sensor-based systems, signal-based systems, or a mixture of both [2]. While global navigation satellite systems (GNSS) could provide centimeter-accurate positioning in open-sky outdoor environments, GNSS signals are unreliable or unusable altogether in other environments (e.g., indoors, deep urban canyons, or jammed environments).

Sensors, such as cameras [3], lasers [4], odometers [5], and inertial measurement units [6], could be used to extract *relative* motion information. However, these are dead-reckoning systems; therefore, during prolonged periods of GNSS outage, the error will accumulate and eventually diverge. Moreover, these sensors only provide *local* position estimates and may not properly function in all environments (e.g., fog, snow, rain, dust, nighttime, etc.).

Signal-based approaches provide the navigation solution in a global frame and do not suffer from the shortcomings of sensor-based systems [7]–[9]. However, signals are challenged in deep urban canyons and indoor environments due to attenuation and multipath, which biases the navigation solution by up to tens of meters [10]–[12]. The effect of multipath has been extensively studied in the literature. Multipath mitigation could be performed at the radio front-end stage using customized antennas (also known as smart antennas) [13]. Other approaches mitigate multipath at the receiver design level using advanced signal processing techniques, such as adaptive signal-to-noise (SNR) [14], cell-averaging constant false alarm rate (CA-CFAR) [15], and correlation techniques [16]. Recent studies have considered multipath mitigation via machine learning (ML). In [17], a nonlinear ML-based model was developed to mitigate periodic GPS multipath signals. ML has been also applied to identify non-line-of-sight (NLOS) conditions [18]. However, identifying NLOS is insufficient to produce a reliable navigation solution.

Multipath can also be mitigated via spatial discrimination of incoming signals via beamforming. Spatial discrimination can be applied to geometrically-diverse signals, which are collected using physical antenna arrays [19], [20] or via synthetic aperture navigation (SAN) frameworks [21]–[24]. Spatial discrimination techniques rely on the ability of beamforming towards the LOS direction while mitigating the multipath components. Spatial discrimination is becoming prevalent with the development of new radio systems (e.g., 5G) and multiple-input-multiple-output (MIMO) systems.

Spatial discrimination is limited by the accuracy of the beamforming steps. This limitation can be related to the model representation and the limited number of features therein. In ML language, this is known as representation learning. A representation learning algorithm can extract the features for a task using datasets, where designing these features manually for nonlinear complex tasks may take decades and an entire community of researchers [25].

This paper proposes a deep learning-aided spatial discriminator for multipath mitigation. The proposed approach is signal-agnostic – it can be applied to a wide range of radio navigation signals. This paper makes the following four contributions: (i) design of cascaded deep neural networks (DNNs) to perform the first three steps of the beamforming process: preprocess filtering, model order estimation (MOE), and direction-of-arrival (DOA) estimation; (ii) extraction of

This work was performed under the financial assistance award 70NANB17H192 from U.S. Department of Commerce, National Institute of Standards and Technology (NIST).

features corresponding to beamforming components using the trained DNNs; (iii) development of an approach to generate reliable datasets that can be used for training the proposed DNNs; and (iv) experimental validation of the proposed approach in four different multipath-rich environments corresponding to indoor pedestrian navigation and ground vehicle urban navigation with cellular long-term evolution (LTE) signals. The proposed system exhibited an *unprecedented* level of accuracy for exploiting cellular LTE signals *exclusively* for navigation *without* fusing any additional signals or sensors, producing position root mean-squared error (RMSE) of 1.67 m, 3.38 m, 1.73 m, and 2.16 m in the four test environments.

The remainder of the paper is organized as follows. Section II presents technical background about: (i) conventional beamforming processes for a uniform linear array (ULA) and (ii) deep learning. Section III discusses the design and training process of the proposed DNNs. Section IV presents the navigation framework, in which the proposed DDN-based beamforming process is integrated into an LTE navigation system. Section V assesses the performance of the proposed DNN-based MOE versus the conventional approaches of minimum description length (MDL) criterion and Akaike information criterion (AIC). Section VI presents experimental results corresponding to four experimental sets, specifically: three indoor experiments and one outdoor experiment, all using LTE signals. Section VII concludes the paper.

II. Background

This section gives necessary background about spatial discrimination and deep learning.

A. ULA-Based Spatial Discrimination

One popular antenna array design for signal classification is the ULA. The classification, as mentioned before, can be done using physical antenna arrays or an SAN approach. The ULA scheme for both scenarios is shown in Fig. 1 [24]. The received signal at the n-th antenna element (or snapshot) is a column vector denoted by $\boldsymbol{x}_n \in \mathbb{R}^{N_s}$, where N_s is the number of samples. The complex representation of the data received by the entire ULA of size N is stacked in $\mathbf{X} \in \mathbb{R}^{N \times N_s}$ as

$$\mathbf{X} = \left[\boldsymbol{x}_1^{\mathsf{T}}, \boldsymbol{x}_2^{\mathsf{T}}, \cdots, \boldsymbol{x}_N^{\mathsf{T}}\right]^{\mathsf{T}}, \tag{1}$$

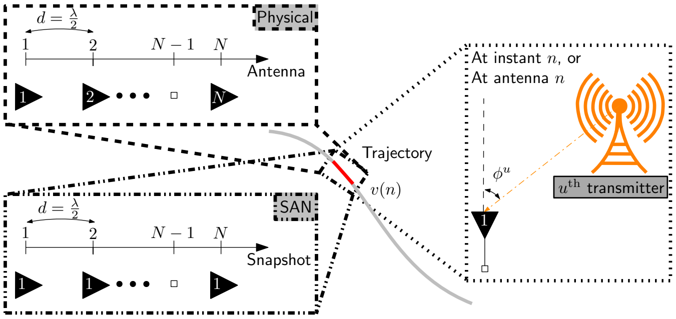

Fig. 1. ULA design for both physical and SAN antenna arrays.

To produce more accurate navigation observables, spatial classification of incoming signals can be exploited to suppress multipath components. To this end, the beamforming process steers the beam towards the LOS direction while nulling the other directions to minimize the effect of multipath. The block diagram in Fig. 2 shows the four main stages of the beamforming process: (i) preprocessing filter, (ii) MOE, (iii) DOA estimator, and (iv) weights generator.

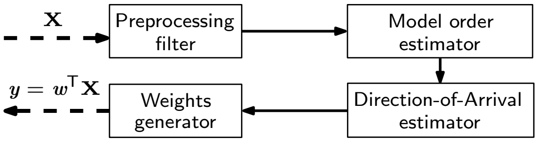
$\mathbf{X}$
Preprocessing filter
Model order estimator
$y = \boldsymbol{w}^{\mathsf{T}}\mathbf{X}$
Weights generator
Direction-of-Arrival estimator

Fig. 2. The four stages of multipath mitigation-based beamforming.

In the first stage, the data is collected as shown in (1) and the data covariance matrix is estimated as

$$\hat{\mathbf{R}}_{xx} = \frac{1}{N_s}\mathbf{X}\mathbf{X}^{\mathsf{H}}, \tag{2}$$

where the space spanned by its eigenvectors can be divided into two orthogonal subspaces: signal subspace and noise subspace. In the preprocessing stage, the data is processed to resolve for the correlation between the incoming signals, at a cost of decreasing the degree-of-freedom (DOF) of the system, i.e., the number of received multipath signals that could be estimated effectively. Spatial smoothing is a conventional approach for preprocessing, which divides the antenna array into a smaller number of subarrays and the estimated data covariance matrices obtained from each subarray are averaged. For ULA, the array is divided into $N_{sub} = N - C + 1$ subarrays to decouple the eigenvectors of at most C coherent signals. The spatially smoothed data is expressed as

$$\mathbf{X}_{ss} = \left[\mathbf{X}_{fss} \; \mathbf{X}_{bss}\right],$$

where $\mathbf{X}_{fss}$ and $\mathbf{X}_{bss}$ are the forward and the backward spatially smoothed data, respectively, defined as

$$\begin{aligned}
\mathbf{X}_{fss} &= \left[\mathbf{J}_{f_1}\mathbf{X} \; \mathbf{J}_{f_2}\mathbf{X} \; \cdots \; \mathbf{J}_{f_C}\mathbf{X}\right], \\
\mathbf{X}_{bss} &= \left[\mathbf{J}_{b1}\mathbf{X} \; \mathbf{J}_{b2}\mathbf{X} \; \cdots \; \mathbf{J}_{bC}\mathbf{X}\right],
\end{aligned}$$

$$\begin{aligned}
\mathbf{J}_{f_c} &= \left[\mathbf{0}_{N_{sub}\times(c-1)} \; \mathbf{I}_{N_{sub}} \; \mathbf{0}_{N_{sub}\times(N-N_{sub}-c+1)}\right] \in \mathbb{R}^{N_{sub}\times N} \\
\mathbf{J}_{bc} &= \left[\mathbf{0}_{N_{sub}\times(N-N_{sub}-c+1)} \; \mathbf{I}_{N_{sub}} \; \mathbf{0}_{N_{sub}\times(c-1)}\right] \in \mathbb{R}^{N_{sub}\times N} \\
&\text{for} \qquad c = 1, \cdots, C.
\end{aligned}$$

Then, the corresponding forward and backward spatially smoothed data covariance matrices are estimated as

$$\begin{aligned}
\hat{\mathbf{R}}_{xx}^{fss} &= \frac{1}{CN_s}\mathbf{X}_{fss}\mathbf{X}_{fss}^{\mathsf{H}} \\
\hat{\mathbf{R}}_{xx}^{bss} &= \frac{1}{CN_s}\mathbf{X}_{bss}\mathbf{X}_{bss}^{\mathsf{H}}.
\end{aligned}$$

Finally, the overall spatially smoothed data covariance matrix is obtained by averaging both the forward and backward subarrays as

$$\hat{\mathbf{R}}_{xx}^{ss} = \frac{1}{2}\left(\hat{\mathbf{R}}_{xx}^{fss} + \hat{\mathbf{R}}_{xx}^{bss}\right). \tag{3}$$

For simplicity, the superscript "^{ss}" is dropped for the rest of the paper; however, the spatially smoothed data is used at any further stage.

In the second stage, the system order is estimated, i.e., the number of incoming signals. A classical technique to estimate the order of the system is to estimate the number of repeated small eigenvalues q (corresponding to the noise subspace) of $\hat{\mathbf{R}}_{xx}$, which theoretically, have the minimum value of the noise variance. In other words, the remaining large M eigenvalues of $\hat{\mathbf{R}}_{xx}$ correspond to the signal subspace and can obtained directly as $M = N - q$. In practice, the smallest eigenvalues representing the noise power will not be identical; instead, they will appear as a closely spaced cluster. This makes it practically impossible to find the q using the classical approach and requires more advanced approaches to perform the task. To this end, two well-known criteria to estimate the order of the system are the minimum description length (MDL) criterion and the Akaike information criterion (AIC) [26], [27]. The estimate $\hat{M}$ of the incoming signals can be expressed as $\hat{M} =$ argmin J, where

$$J = \begin{cases} -\ln\left[\dfrac{\prod_{i=M}^{N} \lambda_i^{\frac{1}{N-M-1}}}{\frac{1}{N-M-1}\sum_{i=M+2}^{N} \lambda_i}\right]^{(N-M-1)N_s} + \hat{p}_m, & \text{MDL} \\ -\ln\left[\dfrac{\prod_{i=M+2}^{N} \lambda_i^{\frac{1}{N-M-1}}}{\frac{1}{N-M-1}\sum_{i=M+2}^{N} \lambda_i}\right]^{(N-M-1)N_s} + \hat{p}_a, & \text{AIC,} \end{cases}$$

where $\hat{p}_m$ and $\hat{p}_a$ are penalty functions [28].

In the third stage, the DOA of incoming signals is estimated. This can be accomplished via the estimation of signal parameters via rotational invariance techniques (ESPRIT) algorithm, which has relatively low computational cost and high resolution. ESPRIT relies on the symmetric properties and the invariance transformation characteristic of the applied antenna array design (e.g., ULA). Algorithm 1 summarizes the steps for the standard ESPRIT algorithm. Further details about ESPRIT can be found in [29].

Algorithm 1 Standard ESPRIT Algorithm [29]

```
1. Perform singular value decomposition $\mathbf{X} = \mathbf{U}\mathbf{\Sigma}\mathbf{V}^{\mathsf{H}}$ and compute $\mathbf{U}_s$ with the $(\hat{M}+1)$ dominant left singular values
2. Solve via total least squares, the invariance equation
       $\mathbf{J}_1\mathbf{U}_s\mathbf{\Psi} = \mathbf{J}_2\mathbf{U}_s,$
       $\mathbf{J}_1 = [\mathbf{I}_{N-1\times N-1}\ \mathbf{0}_{N-1\times 1}]$ and $\mathbf{J}_2 = [\mathbf{0}_{N-1\times 1}\ \mathbf{I}_{N-1\times N-1}]$
3. Calculate the eigenvalues of the resulting complex-valued solution
       $\mathbf{\Psi} = \mathbf{T}\mathbf{\Phi}\mathbf{T}^{-1}, \quad \text{with } \mathbf{\Phi} = \operatorname{diag}[\phi_1, \cdots, \phi_D].$
4. Extract the angular information via
       $\mu_m = \arg(\phi_d), \quad 1 \le m \le (\hat{M}+1)$
       $\phi_m = \arcsin\left(-\frac{-\lambda}{2\pi m}\mu_m\right).$
```

In the last stage, the weighing vector $\boldsymbol{w}$ of the antenna elements is generated to steer the antenna array towards the LOS while suppressing multipath signals. The beamformed output can be expressed as

$$\boldsymbol{y} = \boldsymbol{w}^{\mathsf{H}}\mathbf{X}, \tag{4}$$

The weighing vector can be generated using different beamformers; inhere, Capon's beamformer is adopted according to [19] as

$$\boldsymbol{w} = \frac{\hat{\mathbf{R}}_{xx}^{-1}\boldsymbol{a}_0(\phi)}{\boldsymbol{a}_0^{\mathbf{H}}(\phi)\hat{\mathbf{R}}_{xx}^{-1}\boldsymbol{a}_0(\phi)}, \tag{5}$$

where $\boldsymbol{a}_0$ is the LOS steering vector and computed as

$$\boldsymbol{a}_0 = \left[1, e^{j\mu_u}, \cdots, e^{(N-1)j\mu_u}\right]^{\mathsf{T}},$$

where $\mu_u = -\frac{2\pi}{\lambda} d\sin(\theta_u)$ is the spatial frequency associated with the u-th transmitter.

B. Deep Learning

This section gives an overview of ML application for spatial discrimination to mitigate multipath. ML relies on patterns and inferences of data sets to build a mathematical model to be used to perform a specific task. The ML DNN can be trained in supervised or unsupervised learning fashions to make predictions and decisions. In supervised learning, each instance in the data set is associated with a target, while in unsupervised learning, the DNN learns the data sets that have many features and tries to extract useful properties that allows it to structure its target. In this paper's context, the training instances are associated with a specific output (i.e., system order or DOAs); thus, supervised learning is adopted. Any ML algorithm could be broken into three parts: task T, performance P, and experience E [25].

The machine learning task T describes how the system should process a collection of features captured in organized datasets. A sample in a data set is represented as a vector $\boldsymbol{i} \in \mathbb{C}^n$ where each entry i_j of the vector is a feature. Defining the features of the data in the system can be as easy as choosing the pixel values in an image as the feature or can much more involved in other application. The two common challenges in T are: (1) the number of variables capturing the features and (2) the corresponding size of the network required to avoid overfitting of uninformative inputs or underfitting if some features are missing due to missing inputs. This paper proposes two different DNNs which perform two different tasks: (i) estimate the system order and (ii) estimate the DOAs of incoming signals impinging on the antenna array. In ML language, the first task is considered to be a purely "regression" task between the input vector $\boldsymbol{i}_1$ and the output o_1. The second task is a mix of "regression" and "structured output" tasks, where input $\boldsymbol{i}_2$ and output $\boldsymbol{o}_2$ are both vectors; however, the output here does not need to be fully structured together, i.e., the output elements do not require to be in a chronological order.

The performance P is needed to evaluate the abilities of a proposed ML system. The performance measure is specific to the task under consideration. The performance of different tasks could be measured using different performance metrics (e.g., accuracy of the model, error rate, average-log probability, etc.). In the proposed approach, while the target to be estimated is known, it is impractical to measure the true states of multipath components. Thus, an alternative criterion should be considered. To this end, the normalized squared error is used to evaluate the training stage and a test set of data that is separate from the data used for training the ML is applied to the trained network to assess performance. Also, the DOA of LOS signals of known transmitters (not multipath components) are known and can be used to provide a performance measure on the trained DNN.

The core of the ML system is the experience E, also known as the training process. The experience can be categorized into supervised and unsupervised. The proposed system is a supervised system, where the dataset is pre-defined and the training is performed once for each network using the entire training dataset. The dataset experienced by the learning algorithm contains the feature in each sample, where each sample is associated with a target. A challenge in real-world applications is to generate appropriate datasets that capture real scenarios. This challenge is particularly significant in signal-based applications, considered in this paper, due to the multitude of factors that can affect the observed data. This paper develops an approach to generate reliable datasets to train the DNNs and studies the most significant factors that affects the DNNs' design. This proposed DNNs will be trained using the backpropagation algorithm, summarized in Algorithm 2. The backpropagation algorithm is used to find each weights' contribution with respect to the error function and it minimizes a pre-defined error metric E as $\partial E/\partial\theta_{i,j}^{(k)}$; where $\theta_{i,j}^{k}$ is the weight between j-th neuron in $(k-1)$-th layer and i-th neuron in k-th layer. The following notation will be used: the superscripts "$^{(o)}$" and "$^{(l)}$" denotes the output and l-th layer, respectively, $a_i^{(k)}$ denotes the activation function of i-th neuron in k-th layer, $z_i^{(k)}$ denotes the output of the neuron before applying the activation function, $\delta_i^{(k)} = \partial E/\partial z_i^{(k)}$ which called the delta error, and $w_{i,j}^{(k-1),(k)}$ denotes the weight between the i-th neuron in the $(k-1)$-th layer and j-th neuron in the k-th layer.

III. DNN: Design and Training

This section presents the training process, design, and computational cost of the proposed DNNs.

A. Training Process

Backpropagation is used as a training algorithm. For the training datasets, it is impossible to generate real datasets from real experiments due to the intractable properties of such data. Specifically, it is virtually impossible to get the true order of the system and the DOA of incoming signals in a real multipath scenario. An alternative solution is to rely on simulating datasets that describe real scenarios as much as possible. As a proof of concept, this paper bases its analysis using simulated and real LTE signals. It is worth mentioning that the proposed approach is agnostic to the signal type, and the proposed approach can be applied to other signals, e.g., GNSS, 5G, digital television, etc. This paper considers three multipath-challenging environments: (i) indoor office building (IOB), (ii) indoor open ceiling (IOC), and (iii) outdoor urban area (OUA).

Algorithm 2 Backpropagation Algorithm [30]

1. Initialize the process and calculate the error at the output layer K

$$\delta^{(o)} = \nabla_a^{(o)} \odot g^{'}(z^{(o)}), \tag{6}$$

where $\odot$ is the Hadamard product, $\boldsymbol{g}^{'}(z^{(o)})$ is the partial derivative of the composite activation functions for all neurons at output layer, and $\nabla_a^{(o)}$ is a gradient vector for the output layer.

2. Propagate the error back as

$$\delta^{(l)} = ({\theta^{(l+1)}}^{\mathsf{T}}\delta^{(l+1)}) \odot g^{'}(z^{(l)}). \tag{7}$$

3. Calculate the rate of error as

$$\frac{\partial E}{\partial\theta_{i,j}^{(l)}} = a_j^{(k-1)}\delta_i^{(l)}, \tag{8}$$

where $a_j^{(l-1)}$ reveals the stimulation of each neuron.

4. Update the weights as follows

$$w_{i,j}^{(l-1),(l)} = w_{i,j}^{(l-1),(l)} - \nu\frac{\partial E}{\partial w_{i,j}^{(l-1),(l)}}, \tag{9}$$

where ν is the learning rate.

For the purpose of generating reliable training datasets, an LTE simulator was developed to provide high fidelity channel impulse response (CIR) estimates. The block diagram of the simulator is presented in Fig. 3. The simulator has two stage: (i) user interface and (ii) LTE signals simulation. In the first stage, the user sets the receiver's trajectory and dynamics in a locally-generated map, along with the LTE base stations' (also known as evolved Node Bs or eNodeBs) positions, carrier frequency f_c, and bandwidth. The LTE bandwidth can take different values between 1.4 to 20 MHz [31]. The channel parameters are defined based on the chosen environment among the three aforementioned scenarios. The channel parameters include path loss exponent, shadowing standard deviation, and multipath parameters.

In the second stage, the range and Doppler shift time histories are generated for each antenna element of the antenna array based on the pre-defined parameters: trajectory, dynamics, eNodeBs' position, and f_c. A Rician channel model is adopted to describe the wireless channel in which signals are propagating, where the received signal can be expressed as

$$x(t) = \sum_{i=0}^{M} a_i \exp(j(2\pi f_c t + \theta_i)), \tag{10}$$

where a_i and θ_i are the amplitude and phase of the i-th multipath signal, respectively; f_c is the carrier frequency of the received signal; $i = 0$ represents the LOS component; and $\theta_0 \equiv 0$. The received complex envelope has a Rician distribution give by

$$p(r) = \frac{r}{\sigma^2}e^{\frac{(r^2+A^2)}{2\sigma^2}}I_0(\frac{rA}{\sigma^2}), \tag{11}$$

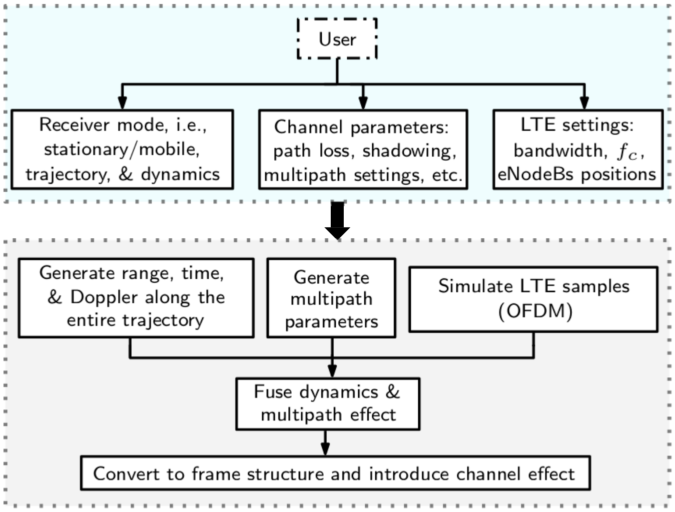
User
Receiver mode, i.e., stationary/mobile, trajectory, & dynamics
Channel parameters: path loss, shadowing, multipath settings, etc.
LTE settings: bandwidth, f_c, eNodeBs positions
Generate range, time, & Doppler along the entire trajectory
Generate multipath parameters
Simulate LTE samples (OFDM)
Fuse dynamics & multipath effect
Convert to frame structure and introduce channel effect

Fig. 3. LTE simulator block diagram

where A is the peak amplitude of the dominant signal, σ^2 is the variance of the multipath components, and I_0 is the zero-order modified Bessel function of the first kind. The Rician factor K is defined as $K = \frac{A^2}{2\sigma^2}$, which is the ratio of the power contributions by LOS to the remaining M multipath components. The RMS delay spread is the square root of the second central moment and is defined as

$$\sigma_{\mathrm{RMS}} = \sqrt{\bar{\tau^2} - (\bar{\tau})^2}, \tag{12}$$

where $\bar{\tau}$ and $\bar{\tau^2}$ are the mean excess delay and the mean square excess delay, respectively. Different multipath environments are represented using different parameters, specifically by varying K and σ. To this end, LTE channel characterization from the literature are used to set K_i and σ_i for $i \in \{\mathrm{IOB}, \mathrm{IOC}, \mathrm{OUA}\}$ [32]–[34]. Table I summarizes the simulation parameters for the different environments.

Next, the LTE reference signals are generated, namely, primary synchronization signal (PSS), secondary synchronization signal (SSS), and cell-specific reference signals (CRS). The CRS will be used later to estimate the CIR, which has the same bandwidth as the LTE system (up to 20 MHz). The generated LTE samples are fused with the computed range and Doppler shifts, and multipath components are merged for each antenna element along with LOS component at each time instance. Then, the signals are converted to frame structure and other channel effects are introduced, namely., noise, path loss, and shadowing; which differ from one environment to another as shown in Table I.

B. DNN Design

DNN design requires defining the terms that characterize its performance and shape as follows:

- Depth: the total number of layers in the network (excluding the input layer). A network with one hidden layer is called a 2-layer DNN.
- Width: the number of neurons in each layer
- Size: the total number of neurons in the network
- Architecture: the connections between different layer and nodes in the network
- Capacity representation: the functions that the network is capable of learning.

TABLE I
LTE CHANNEL PARAMETERS FOR DIFFERENT ENVIRONMENTS

Parameter	**Indoor Office Building**	**Indoor Open Ceiling**	**Outdoor Urban Area**
K-factor	0–0.5	0.5–1	1–2
RMS delay spread	200–250 ns	1–5 μs	10–20 μs
Path loss exponenet	3	2.7	2.4
Shadowing standard deviation [dB]	10	8	4

To characterize the proposed DNNs, the aforementioned terms needs to be determined. It is worth mentioning that there is no analytical way to find the optimal number of layers and the number of the neuron for each layer when designing an artificial network. One way to address this challenge is to predict a specific model via experimentation, which is mainly by following a sequence of experiments to discover what works the best. Recent studies showed that one of the aforementioned terms can be traced in some applications, which is the depth of the model [25]. The depth of the model can be set based on the number of sequential instructions that must be executed in the conventional architecture. The design of the proposed DNNs is discussed next: (i) DNN-based MOE and (ii) DNN-based DOA estimator.

1) DNN-MOE: Conventional model order estimators like MDL and AIC perform a 2-D clustering of the eigenvalues of the estimated data covariance matrix and divide the spanned space into two subsets: signals subspace and noise subspace. Then, the minimum depth of the proposed DNN-MOE can be achieved by a 2-layer MLP. However, this is assuming that the DNN is going to learn the same model, which is neither necessarily nor desirable. Thus, experimentation is performed to evaluate the optimal size of the proposed network. To do so, an incremental order selection (IOS) algorithm is applied, in which the size of the DNN started with 1-2-DNN[1] and increased gradually to 50-25-DNN. For each training configuration, the following is adopted:

- The stopping criterion is determined when the gradient norm is less than a pre-defined threshold.
- The samples are divided into 60% for training, 20 % for testing, and 20% for selection; where selection data is used to determine how the network performs with new data which determines the generality of the trained DNN.
- The final training error and the final selection error were recorded to measure how successful the training is and how the network performs with new data, respectively.

The above training procedure was applied for each of the three environments. Table I summarizes the DNN design

[1] i-j-DNN denotes a DNN with j layers and i neurons in each layer

settings. Each of the three environments has eight datasets corresponding to $N \in \{4, 8, 12, \cdots, 32\}$ antenna array sizes. Each sample in the datasets was chosen randomly from a uniform distribution with support 1 through N. The upper limit N was chosen to enable fair comparison with conventional model order estimators: MDL and AIC. The final selection and training errors for a specific size were averaged over the eight datasets, in order to find a sub-optimal design that is applicable to different antenna array sizes. For each dataset, the input vector $\boldsymbol{i}_{1,N}$ is of length N, and contains the eigenvalues of the estimated data covariance matrix.

Fig. 4 illustrates the training results, from which the following can be concluded:

- Two-layer DNNs with different number of neurons appear to be a good design for the DNN-MOE, since such DNNS have low final training and selection errors (but with different number of neurons).
- The training and selection errors increase approximately monotonically with the size of the DNN.
- The errors start to increase significantly as the DNN size increases, which can be explained due to oversized DNN and the overfitting of training process.

In light of these results, one can identify the DNNs yielding the minimum errors in each of these environments with their corresponding training results as shown in Table III.

TABLE II
DNN Design Settings

Parameter	Value
Number of datasets	8
Number of samples per data set	1000
Size of antenna array	$N = 4, 8, 12, \cdots, 32$
Order of the system	$M \sim U(1, N)$
Gradient norm threshold	1×10^{-4}
Maximum number of training epochs	1000

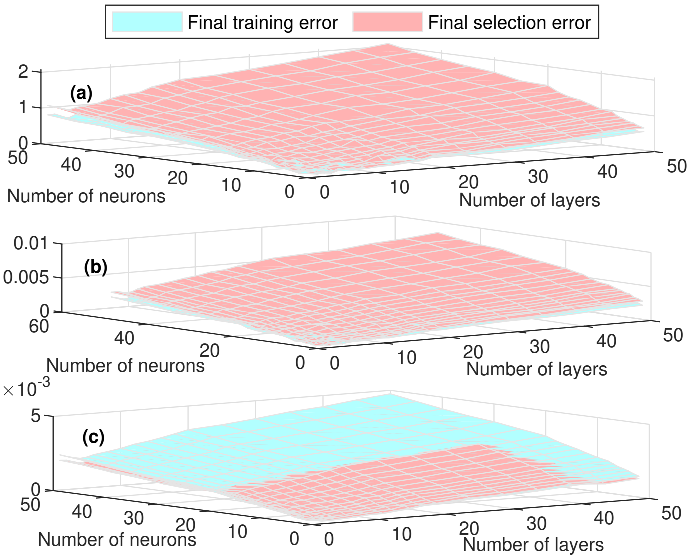

Fig. 4. The final training error and selection error of the proposed DNN-MOE for different number of layers and neurons: (a) IOB, (b) IOC, (c) OUA.

TABLE III
Optimal Design and Training Characteristics of DNN-MOE

Environment	Optimal design	Optimal learning rate ν	Normalized squared error	Number of training epochs
IOB	4-2-DNN	1.4×10^{-4}	0.00265	242
IOC	3-2-DNN	3.2×10^{-4}	0.00218	178
OUA	2-3-DNN	3.7×10^{-4}	0.00202	79

2) DNN-DOAE: For conventional DOA estimators, e.g., the standard ESPRIT algorithm, it is virtually impossible to track the number of sequential instructions required to produce DOA estimates given the eigenvectors of the data covariance matrix. This rises the importance of experimentation in designing the DNN and come up with a sub-optimal design for the proposed DNN-DOAE. The DNN-DOAE design follows the same steps of the DNN-MOE, except:

- The input vector contains the eigenvectors of the signal subspace, i.e., the eigenvectors corresponding to the largest $(\hat{M} + 1)$, where $\hat{M}$ is the system order that has been estimated by the proposed DNN-MOE. The size of the input vector $\boldsymbol{i}_{2,N}$ is $2(\hat{M} + 1)N$, where the “2” appears here due to complex-valued elements, as each element is divided into 2 real-valued inputs in the DNN.
- The input vector does not include the eigenvectors of the noise subspace. The reason for this was that once the noise subspace was included, the DNN training process never converged. This could be justified by knowing that the DNN was trying to capture the correlations between the noise subspace and the DOA estimates, which do not exist.

The DNN-DOAE settings are identical to these of the DNN-MOE shown in Table II. Fig. 5 illustrates the training results, from which the following can be concluded:

- The DNN-DOAE results in higher training and selection errors, which can be justified due to the nature and complexity of the task compared to the previous one.
- Unlike DNN-MOE, the errors here possess a nonmonotonic behavior, where it starts high, then decreases as size increases, and at some point, it starts to increase back as the size increases. This convex shape can be justified by the high errors due to underfitting for small DNN sizes and oversized DNN for large sizes.

In contrast to the DNN-MOE results, the minimum training and final errors do not yield the same exact DNN size; however; they point the same region. Table IV presents the optimal design of the proposed DNN-DOAE in different environments and their training results.

C. Computational Cost

One method to assess the efficiency of the DNN is to trace the asymptotic complexity of the network. In this section, the computational complexity is studied based on the size of the input vector $\boldsymbol{i}_{1/2}$, the number of layers denoted by L, the number of neurons in each layer denoted by $n^{(l)}$, and

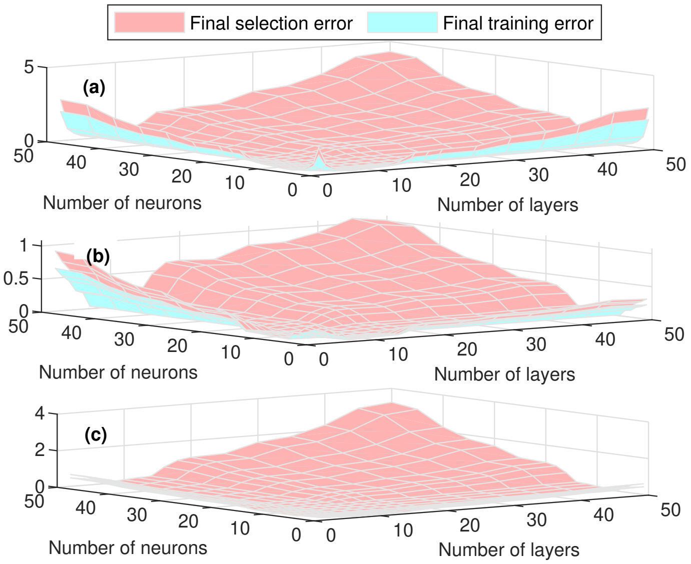

Fig. 5. The final training error and selection error of the proposed DNN-DOAE for different number of layers and neurons: (a) IOB, (b) IOC, (c) OUA.

TABLE IV
OPTIMAL DESIGN AND TRAINING CHARACTERISTICS OF DNN-DOAE

Environment	Optimal design	Optimal learning rate ν	Normalized squared error	Number of training epochs
IOB	5-5-DNN	6.8×10^{-5}	0.0621	418
IOC	3-5-DNN	8.8×10^{-5}	0.0584	333
OUA	8-4-DNN	9.1×10^{-5}	0.0551	287

the backpropagation as a training algorithm with I iterations. Referring to algorithm 2, the input neurons can be treated as any other neuron in the hidden layer with their own activation functions, defined as $a^{(0)}$. The gradient vector run time can be estimated as a constant based on the number of layers as

$$\text{time}\nabla_a = L. \tag{13}$$

The complexity of the delta error for layer "$^{(l)}$" is dependent on the number of neuron $n^{(l)}$ as

$$O(\text{time}_{\delta^{(l)}}) = {n^{(l)}}^2 + {n^{(l)}}^3. \tag{14}$$

Then, the total complexity among all layers is expressed as

$$O(\text{time}_{\delta^{(L)}}) = \sum_{l=0}^{L} ({n^{(l)}}^2 + {n^{(l)}}^3). \tag{15}$$

The run-time complexity of calculating the weights can be ignored with respect to the order of complexity in (15). To this end, the total time complexity after performing I gradient descent iterations and including (13) can be approximated as

$$O(\text{time}_{\text{total}}) = I \cdot \sum_{l=0}^{L} ({n^{(l)}}^2 + {n^{(l)}}^3) + L. \tag{16}$$

IV. NAVIGATION FRAMEWORK AND CASCADED DNN-BASED MULTIPATH MITIGATION

This section presents the navigation framework, which is adapted from the one developed in [23]. The navigation framework block diagram is shown in Fig. 6, which can be divided into three sub-blocks: (i) LTE navigation receiver, (ii) beamformer, and (iii) extended Kalman filter (EKF). The LTE receiver estimates the CIR by tracking the CRS and produces the carrier phase measurements. The CIRs are stacked from N antenna elements, which can correspond to either a physical or a synthetic antenna array [24]. In the beamforming stage, the data covariance matrix is estimated as in (2). For the conventional approach, spatial smoothing is applied and $\hat{M}$ is estimated using either the MDL or AIC criteria, then algorithm 1 is applied to get the DOA estimates. For the proposed DNN approach, the DNN-MOE replaces the prefiltering and the conventional MOEs, and the DNN-DOAE replaces the standard ESPRIT algorithm. Then, the data is beamformed towards the LOS DOA while nulling the multipath components. The beamformed data is fed back to the LTE receiver and corrected carrier phase measurements are produced. In the EKF the stage, the measurements are fed to the EKF to estimate the state vectors

$$\boldsymbol{\zeta} \triangleq \left[\boldsymbol{\zeta}_{\text{rx}}^{\mathsf{T}}, \boldsymbol{\zeta}_{\text{clk}}^{\mathsf{T}}\right]^{\mathsf{T}},$$

where the receiver's position and velocity states are defined as $\boldsymbol{\zeta}_{\text{rx}} \triangleq \left[\boldsymbol{r}^{\mathsf{T}}, \dot{\boldsymbol{r}}^{\mathsf{T}}\right]^{\mathsf{T}}$, and the clock error state vector is defined as $\boldsymbol{\zeta}_{\text{clk}} \triangleq \left[c\delta t_1, c\dot{\delta} t_1, \cdots, c\delta t_U, c\dot{\delta} t_U\right]^{\mathsf{T}}$, where U is the number of eNodeBs, c is the speed of light, and $\{\delta t_u\}_{u=1}^{U}$ and $\{\dot{\delta} t_u\}_{u=1}^{U}$ are the relative clock bias and drift between the receiver and u-th eNodeB. Note that in Fig. 6, k and j are discrete-time instances where $k > j$. The EKF assumes that $\boldsymbol{\zeta}_{\text{rx}}$ evolves according to velocity random walk dynamics while $\boldsymbol{\zeta}_{\text{clk}}$ evolves according to a double integrator driven by process noise [23].

It is worth mentioning that the online computational cost of the DNN-MOE (i.e., after training) is $O(N)$ compared to $O(\text{MDL}) \approx O(\text{AIC}) \approx O\left(\sum_{i=0}^{N-1} \log\left(\frac{1}{N-i}\right) + 2N\right) \approx O\left(2N\right)$.

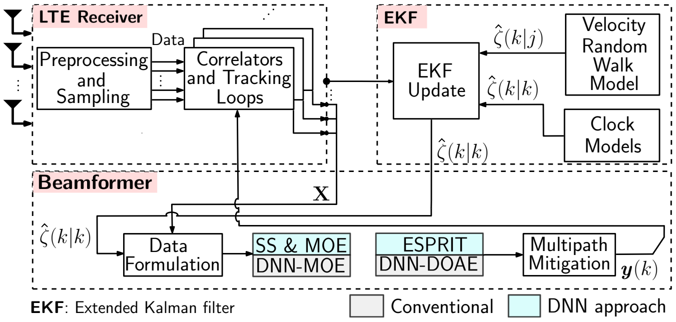

Fig. 6. Navigation framework block diagram

V. MOE: CONVENTIONAL VERSUS DNN-BASED

This section assesses the performance of the proposed DNN-MOE versus conventional approaches. A simulation was conducted (assuming IOB environment) to evaluate the percentage of success of the DNN-MOE in estimating the true

TABLE V
SIMULATION SETTINGS FOR DNN-MOE PERFORMANCE EVALUATION

Case	N	$M_{\max}$	Number of samples
(i)	6	10	5000
(ii)	12	18	5000
(iii)	24	30	5000
(iv)	32	40	5000

order of the system, where four different cases are assumed. Table V summarizes the simulation settings. Fig. 7 presents the performance for different cases and Table VI summarizes the results. In light of these results, the following conclusions can be drawn:

- The proposed DNN-MOE clearly outperforms the MDL and the AIC estimators for $M \leq N$.
- The success rate of MDL and AIC for $M > N$ is zero as expected, where M is greater than the DOF of the array, which is N for both models. However, the DNN-MOE was capable of estimating orders greater than N, even producing comparable success rates compared to $M \leq N$. This result implies that unlike MDL and AIC, the DNN-MOE may not be *just* learning the 2-D clustering of eigenvalues to estimate the order, it could also be performing a higher dimensional clustering where more variations of inputs are represented in the learned model. Another test was performed to encourage/discourage the proposed argument, i.e., the input order selection, which is a method to improve the quality of the predictions by extracting the subset of inputs that have more influence on the learning process. In cases where the trained DNN was constrained to the condition of $M \leq N$, the input selection resulted in excluding few inputs due to their weak influence; however, for $M > N$, the input selection method resulted in including all N inputs, which supports the proposed justification.
- The success rate of DNN-MOE drops for $M \gg N$
- The overall success rate of the proposed DNN-MOE decreases as N increases (still outperforms conventional MOEs). However, for this navigation application, the size of the antenna array is usually not very large due to: (a) focusing on mitigating the most powerful multipath and (b) having size-constraints on navigation devices.

VI. EXPERIMENTAL RESULTS

This section validates the DNN-based beamforming process proposed in Section III. Four experimental studies are presented in which LTE signals are exploited for navigation according to the framework discussed in Section IV in multipath-rich environments. The experiments consider both (i) pedestrian indoor navigation and (ii) ground vehicle urban navigation. Table VII summarizes the experimental environments.

A. Experiment 1: Pedestrian Indoor Navigation with LTE Signals

This subsection presents experimental results in three different IOB environments. For all experiments, the IOB-DNN offline-trained DNNs are applied in the DNN-based beamforming block shown in Fig. 6.

TABLE VI
ORDER ESTIMATION PERFORMANCE COMPARISON

Case	Condition	MDL	AIC	DNN-MOE
(i)	Success for $M \leq N$ [%]	67.56	59.65	99.78
	Success for $M > N$ [%]	0	0	98.75
	Overall Success [%]	37.44	33.06	99.76
(ii)	Success for $M \leq N$ [%]	57.01	52.02	92.65
	Success for $M > N$ [%]	0	0	88.14
	Overall Success [%]	36.60	33.40	90.98
(iii)	Success for $M \leq N$ [%]	41.41	40.7	74.80
	Success for $M > N$ [%]	0	0	65.58
	Overall Success [%]	32.74	32.18	72.92
(iv)	Success for $M \leq N$ [%]	35.03	36.29	62.05
	Success for $M > N$ [%]	0	0	57.29
	Overall Success [%]	27.88	28.88	61.1

TABLE VII
EXPERIMENTAL ENVIRONMENTS

Experiment	Environment	Traversed distance [m]	Duration [s]
1-a	IOB	88.8	49
1-b	IOB	126.8	100
1-c	IOB	109	50
2	OUA	1440	90

1) Experiment 1-a: This experiment was conducted at the Engineering Gateway building in the University of California, Irvine, USA. The pedestrian-mounted receiver receives signals from three U.S. cellular providers: T-Mobile, Verizon, and AT&T, transmitting at four different frequencies, as summarized in Table VIII. Due to hardware limitations, LTE signals for different carrier frequencies were collected in different runs, i.e., the same trajectory was traversed four different times and for each run, the receiver was tuned to a different carrier frequency. The position RMSE between trajectories from different runs referenced to the first trajectory was calculated to be 0.68 m. For each run, the receiver was equipped with two consumer-grade cellular omnidirectional Laird antennas to collect data from the same carrier frequency, which we connected to a dual-channel National Instruments (NI) universal software radio peripherals (USRPs)-2954R to simultaneously down-mix and synchronously sample LTE signals at 20 Msps. The signals were processed in a post-processing fashion using MATLAB. Fig. 8 shows the environment layout in which the experiment was performed, the eNodeBs' positions from which signals were collected, and the experimental hardware and software setup. The ground truth was obtained with a camera that was mounted on the moving cart (facing downward), which was pushed by the pedestrian to record location of specific landmarks placed on the ground with known locations. Fig. 9 shows the receiver's ground truth trajectory versus the navigation solution from: (i) standard SAN-LTE and (ii) the proposed DNN-based SAN framework. Table IX summarizes the experimental results. Fig. 10(i) compares the LOS DOA RMSE of the standard ESPRIT algorithm versus the DNN-DOAE for different LTE eNodeBs over the entire experiment.

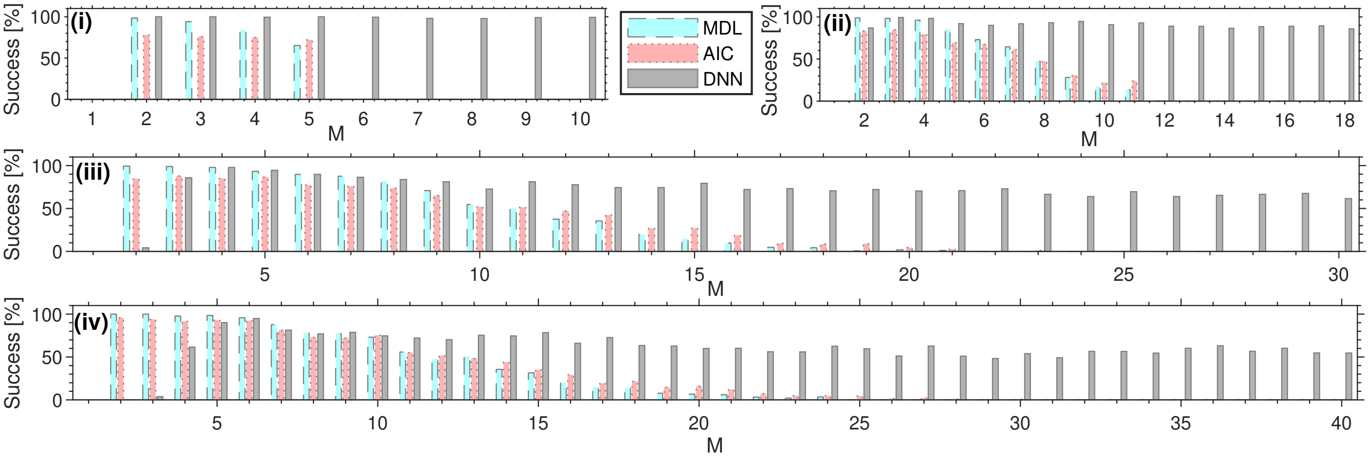

Fig. 7. Success rate for both MDL, AIC, and DNN-MOE versus system order

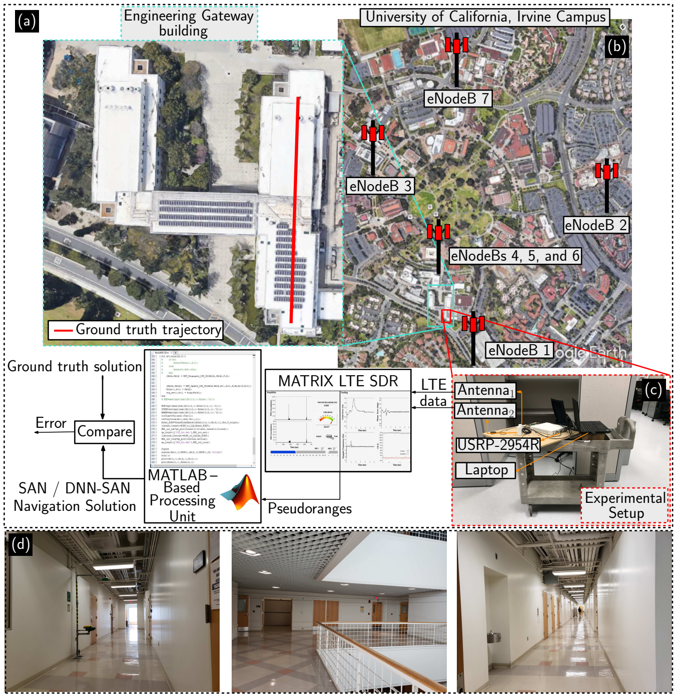

Fig. 8. Environmental layout and experimental setup for experiment 1-a: (a) Engineering Gateway building where the experiment was performed and the ground truth trajectory, (b) LTE eNodeBs' positions, (c) experimental setup, and (d) sample photos of the environment.

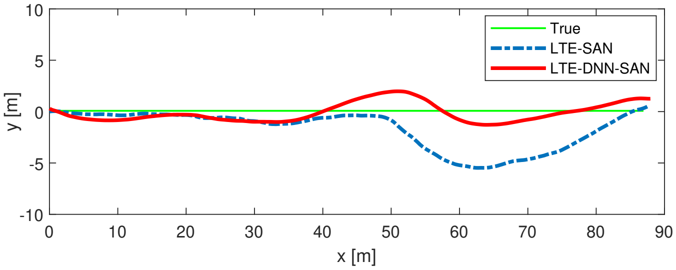

Fig. 9. Navigation solution for experiment 1-a.

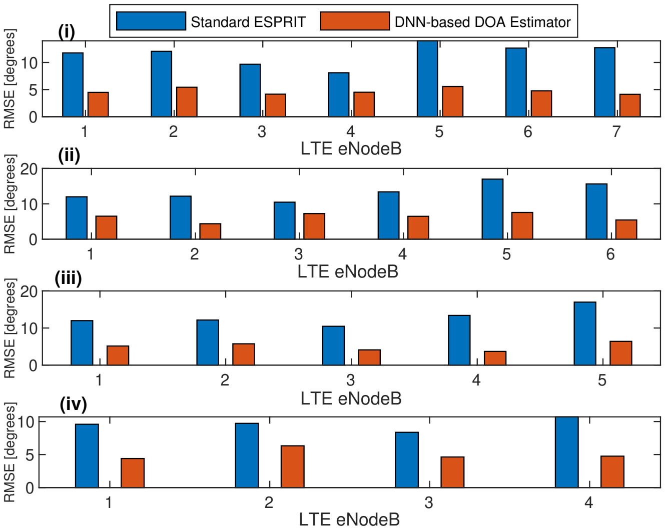

Fig. 10. LOS DOA RMSE comparison of standard ESPRIT versus DNN-based DOA estimator for all experiments and each LTE eNodeB: (i) experiment 1-a, (ii) experiment 1-b, (iii) experiment 1-c, and (iv) experiment 2.

TABLE VIII
LTE eNodeBs' Characteristics: Experiment 1-a

eNodeB	Carrier frequency [MHz]	N_{ID}^{Cell}	Bandwidth [MHz]	Cellular provider
1	1955	11	20	AT&T
2	1955	315	20	AT&T
3	2112.5	178	20	AT&T
4	1955	93	20	AT&T
5	2125	223	20	Verizon
6	2145	394	20	T-Mobile
7	2125	339	20	Verizon

2) *Experiment 1-b:* The second experiment started in one side of the Engineering Gateway building as in Experiment 1-a then transitioned across an indoor bridge connecting the building to another side of the building. A quad-channel NI USRP-2955 was connected to the pedestrian-mounted receiver to sample LTE signals with a sampling rate of 10 Msps. The

TABLE IX
INDOOR POSITIONING PERFORMANCE COMPARISON: EXPERIMENT 1-a

Framework	RMSE [m]	Standard deviation [m]	Maximum error [m]
LTE-SAN	2.62	1.76	5.56
LTE-DNN-SAN	1.67	1.12	3.37

LTE eNodeBs' characteristics are summarized in Table X. The sampled LTE signals were transferred from the USRP-2955 via a PCI Express cable and stored on a laptop for post-processing. Fig. 11 shows the environment layout in which the experiment was performed, the eNodeBs' positions from which signals were collected, and the experimental hardware and software setup. Fig. 12 shows the receiver's ground truth trajectory versus the navigation solution from: (i) standard SAN-LTE and (ii) the proposed DNN-based SAN framework. Table XI summarizes the experimental results. Fig. 10(ii) compares the LOS DOA RMSE of the standard ESPRIT algorithm versus the DNN-DOAE for different LTE eNodeBs over the entire experiment.

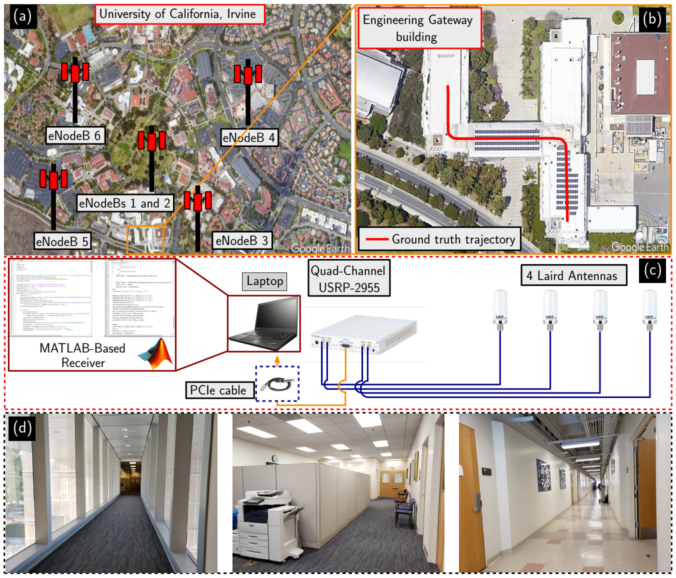

Fig. 11. Environmental layout and experimental setup for experiment 1-b: (a) LTE eNodeBs' positions, (b) Engineering Gateway building where the experiment was performed and the ground truth trajectory, (c) experimental setup, and (d) sample photos of the environment.

TABLE X
LTE ENODEBS' CHARACTERISTICS: EXPERIMENT 1-b

eNodeB	Carrier frequency [MHz]	N_{ID}^{Cell}	Bandwidth [MHz]	Cellular provider
1	1955	93	20	AT&T
2	2125	223	20	Verizon
3	1955	11	20	AT&T
4	1955	198	20	AT&T
5	2145	112	20	T-Mobile
6	2112.5	401	20	AT&T

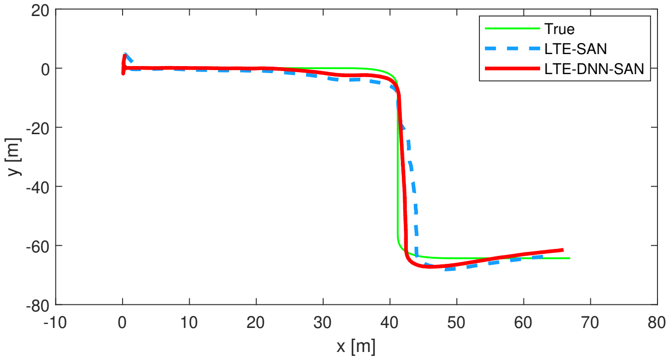

Fig. 12. Navigation solution for experiment 1-b.

TABLE XI
INDOOR POSITIONING PERFORMANCE COMPARISON: EXPERIMENT 1-b

Framework	RMSE [m]	Standard deviation [m]	Maximum error [m]
LTE-SAN	3.93	1.65	5.63
LTE-DNN-SAN	3.38	1.97	5.52

3) Experiment 1-c: This experiment was conducted in the Winston Chung Hall building at the University of California, Riverside, USA. The pedestrian-mounted receiver was equipped with a dual-channel USRP-2954R and two single-channel USRPs-2920. Several tags were placed at known locations on the ground before performing the experiment. Over the course of the experiment, a smart phone camera was used to record the location of the receiver using the tags on the ground, which were later used as the ground truth. Fig. 14 shows the receiver's ground truth trajectory versus the navigation solution from: (i) standard SAN-LTE and (ii) the proposed DNN-based SAN framework. Table XII summarizes the experimental results. Fig. 10(iii) compares the LOS DOA RMSE of the standard ESPRIT algorithm versus the DNN-DOAE for different LTE eNodeBs over the entire experiment.

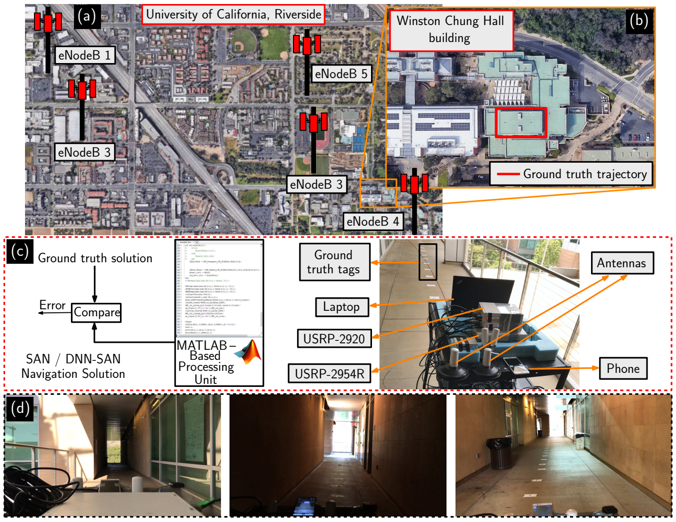

Fig. 13. Environmental layout and experimental setup for experiment 1-c: (a) LTE eNodeBs' positions, (b) Winston Chung Hall building where the experiment was performed and the ground truth trajectory, (c) experimental setup, and (d) sample photos of the environment.

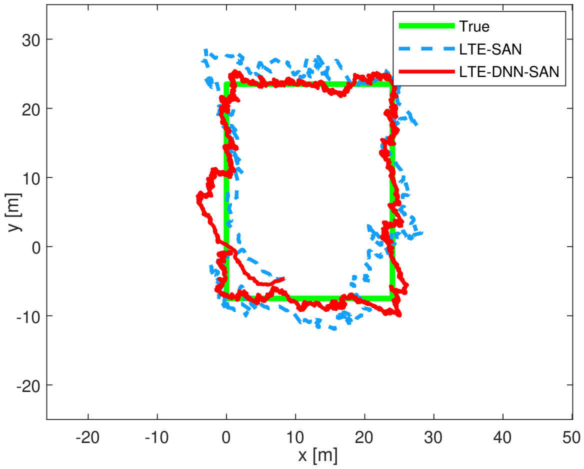

Fig. 14. Navigation solution for experiment 1-c.

TABLE XII
LTE ENODEBS' CHARACTERISTICS: EXPERIMENT 1-C

eNodeB	Carrier frequency [MHz]	N_{ID}^{Cell}	Bandwidth [MHz]	Cellular provider
1	739	144	10	AT&T
2	2145	490	20	T-Mobile
3	1955	262	20	AT&T
4	2145	383	20	T-Mobile
5	751	156	10	Verizon

B. Experiment 2: Ground Vehicle Urban Navigation with LTE Signals

This experiment was conducted in an urban multipath environment: downtown Riverside, CA, USA. The ground vehicle-mounted receiver was receiving signals from four eNodeBs corresponding to the U.S. cellular provider AT&T, transmitting at two different frequencies, as summarized in Table XIV. The receiver was equipped with two consumer-grade cellular omnidirectional Laird antennas and a dual-channel NI USRP-2954R, driven by a GPS-disciplined oscillator (GPSDO) to simultaneously down-mix and synchronously sample LTE signals with 20 Msps. The signals were processed in a post-processing fashion using MATLAB. Fig. 15 shows the experimental hardware and software setup and sample images of the environment. The GPS signal, which was down-mixed and sampled by a single-channel NI USRP-2930m was used later to produce the vehicle's "ground truth" trajectory. Fig. 16 shows the environmental layout, eNodeBs' position, and the receiver's ground truth trajectory versus the navigation solution from: (i) standard SAN-LTE and (ii) the proposed DNN-based SAN framework. Table XV summarizes the experimental results. Fig. 10(iv) compares the LOS DOA RMSE of the standard ESPRIT algorithm versus the DNN-DOAE for different LTE eNodeBs over the entire experiment.

C. Discussion

The previous results clearly demonstrate the efficiency of the proposed DNN-based multipath mitigation approach. It should be noted that these environments are multipath-rich, making them challenging for radio navigation. Nevertheless, the proposed DNN-based approach produced *unprecedently* accurate navigation, exclusively with cellular LTE signals processed with commercial off-the-shelf (COTS) radio frequency front ends, and with fusing any additional sensors or high-end components.

TABLE XIII
INDOOR POSITIONING PERFORMANCE COMPARISON: EXPERIMENT 1-C

Framework	RMSE [m]	Standard deviation [m]	Maximum error [m]
LTE-SAN	4.05	2.43	11.48
LTE-DNN-SAN	1.73	1.22	9.63

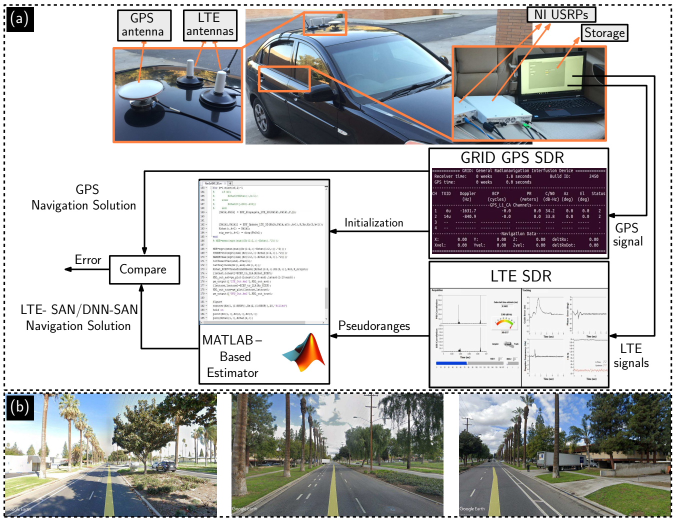

Fig. 15. (a) Experimental setup and (b) sample photos for experiment 2.

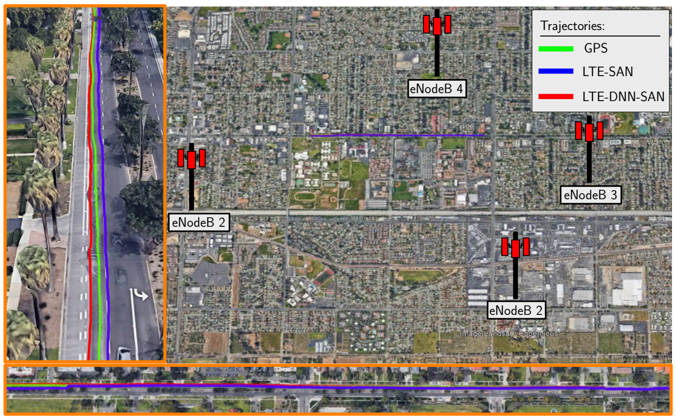

Fig. 16. Environment layout, the eNodeBs' locations, and the traversed trajectory of experiment 2.

VII. CONCLUSION

This paper presented a deep learning-based beamforming approach to mitigate multipath. The proposed approach addresses the limitations of conventional beamforming algorithm by developing a DNN-based model order and DOA estimators to replace the conventional approaches. The training and design processes of the proposed DNNs are discusses for different environments. The paper assesses the performance

TABLE XIV
LTE ENodeBs’ Characteristics: Experiment 2

eNodeB	Carrier frequency [MHz]	N_{ID}^{Cell}	Bandwidth [MHz]	Cellular provider
1	739	152	10	AT&T
2	1955	216	10	AT&T
3	739	232	10	AT&T
4	739	288	10	AT&T

TABLE XV
Indoor Positioning Performance Comparison: Experiment 2

Framework	RMSE [m]	Standard deviation [m]	Maximum error [m]
LTE-SAN	2.74	2.03	8.23
LTE-DNN-SAN	2.16	1.13	4.70

of DNN-based MOE versus the conventional approaches via simulations. The performance of the proposed approach is validated experimentally in four different multipath-rich environments corresponding to pedestrian indoors and ground vehicle urban navigation with cellular LTE signals. The proposed system reduces the position root mean-squared error (RMSE) compared to the state-of-the-art SAN-based beamforming by 36.26%, 13.99%, 57.28%, and 21.17% in the four experiments.

VIII. Acknowledgment

The authors would like to thank Zainab Ashai, Joe Khalife, Kimia Shamaei, Mahdi Maaref, Joshua Morales, and Mohamad Orabi for their help in data collection.

References

[1] Z. Kassas, P. Closas, and J. Gross, “Navigation systems for autonomous and semi-autonomous vehicles: Current trends and future challenges,” *IEEE Aerospace and Electronic Systems Magazine*, vol. 34, no. 5, pp. 82–84, May 2019.

[2] K. Krishnaswamy, S. Susca, R. McCroskey, P. Seiler, J. Lukas, O. Kotaba, V. Bageshwar, and S. Ganguli, “Sensor fusion for GNSS denied navigation,” in *Proceedings of IEEE/ION Position, Location, and Navigation Symposium*, April 2008, pp. 541–551.

[3] M. Li and A. Mourikis, “High-precision, consistent EKF-based visual-inertial odometry,” *International Journal of Robotics Research*, vol. 32, no. 6, pp. 690–711, May 2013.

[4] A. Soloviev, “Tight coupling of GPS, INS, and laser for urban navigation,” *IEEE Transactions on Aerospace and Electronic Systems*, vol. 46, no. 4, pp. 1731–1746, October 2010.

[5] Y. Wu, C. Goodall, and N. El-Sheimy, “Self-calibration for IMU/odometer land navigation: Simulation and test results,” in *Proceedings of ION International Technical Meeting*, 2010, pp. 839–849.

[6] Y. Wang, S. Askari, and A. M. Shkel, “Study on mounting position of IMU for better accuracy of ZUPT-aided pedestrian inertial navigation,” in *IEEE International Symposium on Inertial Sensors and Systems*, April 2019, pp. 1–4.

[7] C. Gentner, E. Munoz, M. Khider, E. Staudinger, S. Sand, and A. Dammann, “Particle filter based positioning with 3GPP-LTE in indoor environments,” in *Proceedings of IEEE/ION Position, Location and Navigation Symposium*, April 2012, pp. 301–308.

[8] Z. Kassas, J. Khalife, K. Shamaei, and J. Morales, “I hear, therefore I know where I am: Compensating for GNSS limitations with cellular signals,” *IEEE Signal Processing Magazine*, pp. 111–124, September 2017.

[9] Z. Kassas, J. Morales, and J. Khalife, “New-age satellite-based navigation – STAN: simultaneous tracking and navigation with LEO satellite signals,” *Inside GNSS Magazine*, vol. 14, no. 4, pp. 56–65, 2019.

[10] Inside GNSS, “Multipath vs. NLOS signals,” insidegnss.com/multipath-vs-nlos-signals/, November 2013.

[11] X. Chen, F. Dovis, S. Peng, and Y. Morton, “Comparative studies of GPS multipath mitigation methods performance,” *IEEE Transactions on Aerospace and Electronic Systems*, vol. 49, no. 3, pp. 1555–1568, July 2013.

[12] K. Shamaei, J. Khalife, and Z. Kassas, “Pseudorange and multipath analysis of positioning with LTE secondary synchronization signals,” in *Proceedings of Wireless Communications and Networking Conference*, April 2018, pp. 286–291.

[13] C. Counselman, “Multipath-rejecting GPS antennas,” *Proceedings of the IEEE*, vol. 1, pp. 86–91, 99 1999.

[14] C. Comp and P. Axelrad, “Adaptive SNR-based carrier phase multipath mitigation technique,” *IEEE Transactions on Aerospace and Electronic Systems*, vol. 34, no. 1, pp. 264–276, January 1998.

[15] K. Shamaei, J. Khalife, and Z. Kassas, “Exploiting LTE signals for navigation: Theory to implementation,” *IEEE Transactions on Wireless Communications*, vol. 17, no. 4, pp. 2173–2189, April 2018.

[16] K. Shamaei and Z. Kassas, “LTE receiver design and multipath analysis for navigation in urban environments,” *NAVIGATION, Journal of the Institute of Navigation*, vol. 65, no. 4, pp. 655–675, December 2018.

[17] H. Phan and S. Tan, “Mitigation of gps periodic multipath using non-linear regression,” in *Proceedings of IEEE European Signal Processing Conference*, August 2011, pp. 1795–1799.

[18] X. Cai, X. Li, R. Yuan, and Y. Hei, “Identification and mitigation of NLOS based on channel state information for indoor WiFi localization,” in *International Conference on Wireless Communications Signal Processing*, October 2015, pp. 1–5.

[19] Z. Chen, G. Gokeda, and Y. Yu, *Introduction to Direction-of-arrival Estimation*. Artech House, 2010.

[20] K. Shamaei, J. Khalife, and Z. Kassas, “A joint TOA and DOA approach for positioning with LTE signals,” in *Proceedings of IEEE/ION Position, Location, and Navigation Symposium*, April 2018, pp. 81–91.

[21] S. Draganov, M. Harlacher, L. Haas, M. Wenske, and C. Schneider, “Synthetic aperture navigation in multipath environments,” *IEEE Wireless Communications*, vol. 18, no. 2, pp. 52–58, April 2011.

[22] S. Daneshmand, A. Broumandan, N. Sokhandan, and G. Lachapelle, “GNSS multipath mitigation with a moving antenna array,” *IEEE Transactions on Aerospace and Electronic Systems*, vol. 49, no. 1, pp. 693–698, January 2013.

[23] A. Abdallah, K. Shamaei, and Z. Kassas, “Indoor localization with LTE carrier phase measurements and synthetic aperture antenna array,” in *Proceedings of ION GNSS Conference*, September 2019, pp. 2670–2679.

[24] A. Abdallah and Z. Kassas, “Evaluation of feedback and feedforward coupling of synthetic aperture navigation with LTE signals,” in *Proceedings of IEEE Vehicular Technology Conference*, September 2019, pp. 1–6.

[25] I. Goodfellow, Y. Bengio, and A. Courville, *Deep learning*. Cambridge, USA: MIT press, 2016.

[26] M. Wax and I. Ziskind, “Detection of the number of coherent signals by the MDL principle,” *IEEE Transactions on Acoustics, Speech, and Signal Processing*, vol. 37, no. 8, pp. 1190–1196, August 1989.

[27] W. Pan, “Akaike’s information criterion in generalized estimating equations,” *Biometrics*, vol. 57, no. 1, pp. 120–125, March 2001.

[28] J. Rissanen, “Modeling by shortest data description,” *Automatica*, vol. 14, no. 5, pp. 465–471, September 2019.

[29] R. Roy and T. Kailath, “ESPRIT-estimation of signal parameters via rotational invariance techniques,” *IEEE Transactions on Acoustics, Speech, and Signal Processing*, vol. 37, no. 7, pp. 984–995, July 1989.

[30] D. Rumelhart, G. Hinton, and R. Williams, “Learning representations by back-propagating errors,” *Nature*, vol. 323, no. 6088, pp. 533–536, October 1986.

[31] 3GPP2, “Physical layer standard for cdma2000 spread spectrum systems (C.S0002-E),” 3rd Generation Partnership Project 2 (3GPP2), TS C.S0002-E, June 2011.

[32] A. Kaya and D. Calin, “Modeling three dimensional channel characteristics in outdoor-to-indoor LTE small cell environments,” in *Proceedings of IEEE Military Communications Conference*, November 2013, pp. 933–938.

[33] Y. Wang, W. Lu, and H. Zhu, “Propagation characteristics of the LTE indoor radio channel with persons at 2.6 GHz,” *IEEE Antennas and Wireless Propagation Letters*, vol. 12, pp. 991–994, 2013.

[34] 3GPP, “Physical channels and modulation,” https://www.etsi.org/deliver/etsi-ts/138200-138299/138211/15.02.00-60/ts-138211v150200p.pdf, 5G; NR; 3rd Generation Partnership Project (3GPP), TS 38.211, July 2018.